UC Riverside
UC Riverside Previously Published Works

Title

RBC-Derived Optical Nanoparticles Remain Stable After a Freeze–Thaw Cycle

Authors

Tang, Jack C
Vankayala, Raviraj
Mac, Jenny T
et al.

Peer reviewed

HHS Public Access

Author manuscript

Langmuir. Author manuscript; available in PMC 2023 January 17.

RBC-Derived Optical Nanoparticles Remain Stable After a Freeze–Thaw Cycle

Jack C. Tang,

Raviraj Vankayala,

Jenny T. Mac,

Bahman Anvari

Department of Bioengineering, University of California, Riverside, California 92521, United States

Abstract

Nanosized carriers engineered from red blood cells (RBCs) provide a means for delivering various cargos, including drugs, biologics, and imaging agents. We have engineered nanosized particles from RBCs, doped with the near-infrared (NIR) fluorochrome, indocyanine green (ICG). An important issue related to clinical translation of RBC-derived nanocarriers, including these NIR nanoparticles, is their stability postfabrication. Freezing may provide a method for long-term storage of these and other RBC-derived nanoparticles. Herein, we have investigated the physical and optical stability of these particles in response to a single freeze–thaw cycle. Nanoparticles were frozen to −20 °C, stored frozen for up to 8 weeks, and then thawed at room temperature. Our results show that the hydrodynamic diameter, zeta potential, optical density, and NIR fluorescence emission of these nanoparticles are retained following the freeze–thaw cycle. The ability of these nanoparticles in NIR fluorescence imaging of ovarian cancer cells, as well as their biodistribution in reticuloendothelial organs of healthy Swiss Webster mice after the freeze–thaw cycle is similar to that for freshly prepared nanoparticles. These results indicate that a single cycle of freezing the RBC-derived nanoparticles to −20 °C followed by thawing at room temperature is an effective method to retain the physical and optical characteristics of the nanoparticles, and their interactions with biological systems without the need for use of cryoprotectants.

Graphical Abstract

Corresponding Author Bahman Anvari – Department of Bioengineering, University of California, Riverside, California 92521, United States; anvarib@ucr.edu.
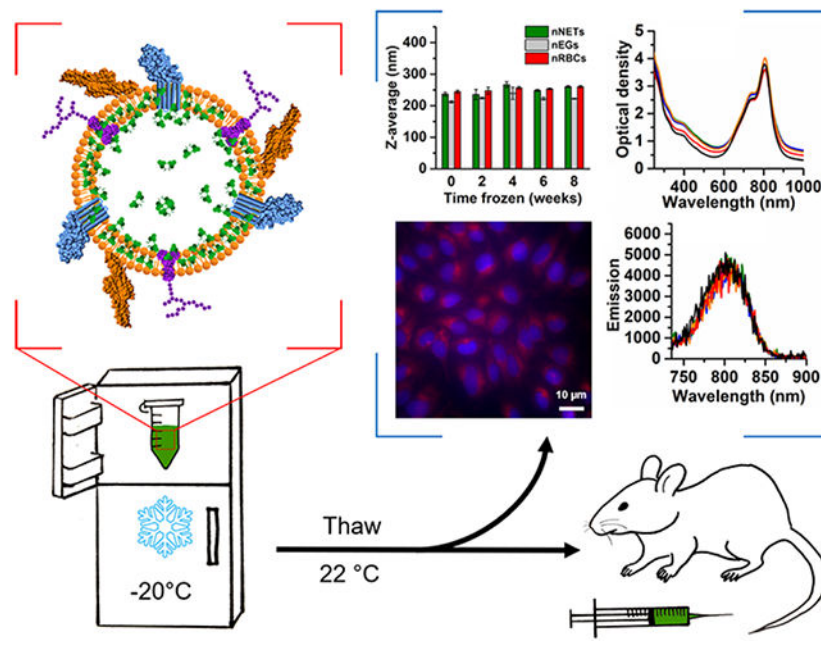
INTRODUCTION

Nanosized carriers engineered from red blood cells (RBCs) provide a means of delivering cargo to desired sites within the body. These delivery systems can be used to enhance the circulation time of the cargo by concealing it within an immuno-privileged construct.[1,2] The RBC membrane contains several immunomodulatory proteins including CD47,[3] CD235a,[4] and CD55,[5,6] which contribute to shielding the cells from phagocytosis and prolonging their circulation.[7] Additionally, animal studies indicate that RBC-derived constructs are potentially nontoxic and biocompatible.[1,2]

Biomedical cargos can range from drugs and biologics[8-11] to optical and magnetic resonance agents.[2,12-15] A particular optical agent is the near-infrared (NIR) dye, indocyanine green (ICG). ICG is currently the only NIR fluorochrome approved by the FDA for specific usage including assessment of cardiac output,[1,17] liver function,[18-20] and retinal angiography.[21-24] There is also an extensive history of ICG usage in investigational clinical studies, including applications in image-guided sentinel lymph node biopsy[25-28] and fluorescence-guided surgery.[29-31]

We provided the first report in encapsulating ICG into nanosized constructs derived from RBCs.[32] We refer to these ICG-loaded RBC carriers as NIR erythrocyte-derived transducers (NETs) since they can transduce the absorbed NIR photons to emit fluorescence, produce reactive oxygen species, or generate heat.[14] In this manner, they serve as potentially useful platforms for broad biomedical imaging and phototherapy of tissue malformations, such as port wine stain,[33] or cancer.[14,32,34]

An important issue related to clinical translation of RBC-derived nanocarriers, including NETs, is their physical and optical stability postfabrication. We previously determined

that NETs fluorescence remained stable for up to at least 12 when maintained at 37 °C (physiological temperature) or stored at 4 °C.[35] RBCs can be stored at 4 °C for up to 6 weeks with the appropriate additives such as saline-adenine-glucose-mannitol.[36] However, refrigerated storage can induce a variety of physicochemical changes to RBCs to affect their function and survival. Freezing of RBCs at −80 °C with the addition of cryoprotectants has been reported as an alternative method to refrigerated storage.[37,38]

Freezing at −20 °C can potentially enable the long-term storage and rapid administration of nanosized NETs (nNETs) for an intended clinical application. Compared to −80 °C storage, facilities for −20 °C storage are inexpensive and readily available in most laboratories and clinical settings. In a previous study, Kuo et al. exposed bovine-derived "nanoerythrosomes" to −20 °C and room temperature (RT) freeze–thaw cycles up to five times and found that these particles had stable diameters upon freeze–thaw cycling.[39]

Herein, we investigate the physical and optical properties of nNETs after a single cycle of frozen storage at −20 °C for various durations up to 8 weeks, followed by subsequent thawing at RT. The eight-week storage time of nNETs at −20 °C is important since it exceeds the current refrigerated storage limitation of 6 weeks for RBCs in the presence of additive solutions.[40] We also evaluate the ability of frozen–thawed nNETs for NIR fluorescence imaging of SKOV3 ovarian cancer cells. We have previously used this cell line to demonstrate the utility of freshly prepared nNETs in cancer cell imaging.[41,42] Finally, we compare the biodistribution of frozen–thawed nNETs (stored at −20 °C overnight) with that of fresh nNETs in healthy Swiss Webster (SW) mice. Our results indicate that the physical and optical characteristics of nNETs, their capability for NIR fluorescence imaging of ovarian cancer, and biodistribution profiles in SW mice are retained after a single cycle of freezing at −20 °C and thawing at RT without using cryoprotectants.

MATERIALS AND METHODS

Fabrication of Nanosized RBC-Derived Particles.

RBCs were isolated from whole human blood (Biological Specialty Company) by centrifugal washing in cold (4 °C) isotonic (~300 mOsm) phosphate-buffered saline (PBS) (referenced as 1× PBS) three times (5 min at 800g). Isolated RBCs were then washed repeatedly in cold 0.25× PBS (20 min, 20,000g) until the supernatant was colorless. The resulting hemoglobin-depleted microsized erythrocyte ghosts (μGs) were then resuspended in 1× PBS, centrifuged once more (20 min, 20,000g), and resuspended in the same volume (1 mL) as the RBCs used.

The μEGs were diluted 1:10 in 1× PBS and serially extruded through polycarbonate membranes with track-etched pore diameters of 800, 400, and 200 nm (Whatman, GE Healthcare) using nitrogen gas pressure in a 10 mL Lipex extruder (Transferra Nanosciences). The samples were passed through each pore size at least three times before reducing the pore size to the next smaller pore diameter. The resulting nanosized EGs (nEGs) were then concentrated 10-fold, back to their original concentration in 1× PBS. nEGs were loaded with ICG by combining 500 ^L of nEGs with 500 μL of 0.1 M Sørensen buffer at pH 7.4 (prepared by combining 19 mL of 0.2 M NaH$_2$PO$_4$ with 81 mL of 0.2 M

Na$_2$HPO$_4$) and then adding 500 μL of 75 μMICG. The final ICG loading concentration in this loading buffer was 25 μM. As control samples, isolated RBCs extruded using the above procedure to form nanosized RBCs (nRBCs), and nEGs without ICG loading were used.

Freeze–Thaw Cycle and Characterizations.

Nanosized RBC-derived particles were cooled from RT at the rate of approximately −1 °C/min in a −20 °C freezer and stored for up to 8 weeks. At biweekly intervals (2, 4, 6, and 8 weeks), frozen aliquots of nNETs were thawed at RT (22 °C) at a warming rate of ≈1.6 °C/min) and characterized within 1 h of thawing. Each aliquot thawed for measurement was not reused. Therefore, each measurement was performed on samples that were stored frozen for the indicated durations, and samples were exposed to only one freeze–thaw cycle prior to characterization.

The cooling rate was calculated based on the known temperature drop from RT 22 to 0 °C and the measured time to freeze the nNETs samples (~20 min). Warming rate was determined from the air-thawing temperature curves reported by Baboo et al.[43] We characterized the RBCs and particles before and after freeze–thawing, as described below.

We acquired UV–vis-NIR spectral data in the range of 230–1000 nm using a spectrophotometer (JASCO V-670, Tokyo, Japan) in transmission mode. Each formulation was diluted 8-fold in 1× PBS prior to the measurements. Samples were placed within a quartz microcuvette (1 cm path length) (Starna Cells, Atascadera, CA) before and after the freeze–thaw cycle. The recorded measurements represent the optical density (OD) of the particle suspension and are a measure of the intensity of the transmitted light after absorption and scattering of the incident light by the particles.

The fluorescence emission spectrum of each formulation was recorded after diluting it 5-fold in 1× PBS. Spectra were acquired using a Horiba Jobin Yvon FluoroLog 3 (Kyoto, Japan) with samples placed within a quartz microcuvette before and after freeze–thaw cycling. The excitation wavelength was 720 nm, selected from a 450 W xenon arc lamp using a monochromator with a slit width of 5 nm. The emission was collected in the range of 735–900 nm.

Using dynamic light scattering (DLS), we quantified the hydrodynamic diameter (Z-average) and the zeta potential (ζ) of RBC-derived nanoparticles (nNETs, nEGs, nRBCs), RBCs, and μEGs using a Malvern Zetasizer NanoZS (Malvern, United Kingdom). DLS has been used to determine the size distributions of RBCs,[44,45] cell lysates,[46] and cell-derived nanoparticles.[47,48] We have previously cross-validated DLS-based measurements of nNETs diameter with electron microscopy measurements and found good agreement between the two methods.[32,41] For DLS-based measurements, samples were suspended in 1 mL of 1× PBS within disposable polystyrene cuvettes (1 cm path length). The Z-average diameters, which are the intensity-weighted harmonic average of the light-scattering particles,[49,50] were estimated at a 90° scattering angle. Each sample was measured eight times, and the average and standard deviation (SD) of these measurements were determined.

Values of ζ were estimated using the Smoluchowski approximation, which assumes the Debye radius to be much smaller than the particle radius.[51] Each measurement was done in a folded capillary cell at 22 °C. The value of ζ for each sample was measured eight times, and the average and SD were determined.

In Vitro NIR Fluorescence Imaging and Uptake by SKOV3 Ovarian Cancer Cells.

SKOV3 ovarian cancer cells were cultured in Roswell Park Memorial Institute (RPMI) 1640 medium supplemented with 10% fetal bovine serum (FBS) and 1% penicillin/streptomycin at 37 °C in a 5% CO_2 atmosphere until confluency. For the uptake study of fresh and frozen–thawed nNETs (stored at −20 °C overnight, thawed at RT), adherent SKOV3 cells were detached using trypsin and seeded at $\approx 1 \times 10^4$ cells per well in a 96-well plate. The cells were then incubated for 2 h at 37 °C with 100 μL of either fresh nNETs (positive control), frozen–thawed nNETs, or isotonic PBS (negative control), and an additional 100 μL of serum-free RPMI 1640.

After incubation, SKOV3 cells were fixed with 4% paraformaldehyde (PFA) and their nuclei were stained with 4′,6-diamidino-2-phenylindole (DAPI). The procedure for fixing SKOV3 cells and nuclear staining was similar to the procedure reported in a prior study.[41] We first removed the media and rinsed the cells in the 96-well plate with 100 μL 1× PBS at 37 °C. We then removed the 1× PBS and incubated the cells in 100 μL 4% PFA for 5 min. The PFA was then removed, and cells were again rinsed with 100 μL of 1× PBS. We again removed the 1× PBS and permeabilized the SKOV3 cells by incubating them in 100 μL of 2% Tween 20 for 5 min. The Tween 20 was removed, and cells were rinsed again with 100 μL 1× PBS. Then we stained the SKOV3 nuclei by first removing 1× PBS and replacing it with 100 μL of 300 nM DAPI dissolved in 1× PBS for 5 min. Following DAPI staining, cells were rinsed twice in 1× PBS and then imaged in 100 μL 1× PBS. We repeated this procedure in four separate wells for imaging and statistical analysis.

In each well ($n = 4$), we recorded fluorescence images of SKOV3 cells that were incubated with either fresh nNETs, frozen–thawed nNETs, or PBS using a Nikon Eclipse Ti microscope (100× magnification) coupled to an electron-multiplying charge-coupled device (Hamamatsu Quant EM-CCD, C9100). We recorded images of the blue-fluorescent nuclei using a Semrock BrightlineDAPI-5060B-NTE filter set and NIR-fluorescent cell bodies using a Chroma 41037 filter set (excitation: 740 ± 17 nm, emission: >780 nm) and superimposed the coregistered images. Average cell fluorescence ($\overline{F}_{\text{cells}}$) was quantified by first summing the NIR signal in the entire field of view (512×512 pixels) in a given image, dividing the summed NIR signal by the number of cells counted by DAPI staining, and then averaging among the number of images:

$$\overline{F}_{\text{cells}} = \frac{1}{n} \sum_{n=1}^{4} \frac{\sum_{x=1}^{512} \sum_{y=1}^{512} F_{\text{NIR}}}{n_{\text{cells}}} \tag{1}$$

where F_{NIR} is the pixel fluorescence intensity in the near-infrared channel, n_{cells} is the number of cell nuclei counted in the DAPI channel, and $n = 4$ (total of four images, one from each well). For each sample (fresh nNETs, frozen–thawed nNETs, or PBS), $\overline{F}_{\text{cells}}$ was

calculated and the standard deviation of $\overline{F}_{cells}$ was computed and presented as error bars in Figure 4d.

Biodistribution of Fresh and Frozen–Thawed nNETs in Healthy SW Mice.

Healthy female SW mice ($\approx$20–25 g; $\approx$8–10 weeks old) were procured (Taconic) and utilized in this study under a protocol approved by the University of California, Riverside Institutional Animal Care and Use Committee. Animals were anesthetized by inhalation of 2% isoflurane in oxygen. We then administered $\approx$100 μL of either fresh or frozen–thawed nNETs (stored at −20 °C overnight, thawed at RT) via tail-vein injection while animals were still under anesthesia ($n = 3$ for each of the administered agents). Eighteen hours postinjection, the mice were euthanized by CO_2 inhalation, and a sample of blood (>500 μL) was immediately drawn from each animal via cardiac puncture. The mice were then dissected and the reticuloendothelial system (RES) organs (liver, lungs, and spleen) were harvested for analysis by fluorescence spectroscopy.

The procedure for measuring the mass-normalized fluorescence of each organ was similar to the procedure detailed in a prior study.[2] Each organ was weighed in a tared microcentrifuge tube and then incubated in 1 mL of 5% sodium dodecyl sulfate (SDS) for 30 min before being homogenized using an Omni Tissue Homogenizer. After homogenization, an additional 4 mL of 5% SDS was added, and the homogenized organs were then incubated for 30 min to allow the release of ICG from cells. The homogenate was centrifuged at 16,000g for 45 min to remove the crude tissue solids from the liquid organ homogenate. Fluorescence spectra of the supernatants were acquired in the range of 735–900 nm in response to 720 nm excitation from a 450 W xenon arc lamp (5 nm slit width).

For each organ, we spectrally integrated the emission spectra and normalized this quantity by the mass of the organ measured. We then divided the result by the number of animals to define the quantity I^*:

$$I^* = \frac{1}{n} \sum_{j=1}^{n} \frac{\int_{735nm}^{900nm} F(\lambda_{em}) d\lambda_{em}}{m_{organ}} \tag{2}$$

where $F(\lambda_{em})$ is the fluorescence intensity at a given emission wavelength λ_{em} and m_{organ} is the mass of the organ. On the basis of this quantity, we obtained the average amount of NIR signal per gram of organ.

The blood samples were treated using the same homogenization protocol and quantitative fluorescence analysis as the organs. After acquisition of the NIR signals generated by the supernatants of homogenized organs or blood, we performed a two-way analysis of variants (ANOVA) to determine if any statistically significant differences in biodistribution originated from freeze–thaw cycling.

RESULTS AND DISCUSSION

Hydrodynamic Diameter and Zeta Potential (ζ) of Frozen–Thawed Particles.

RBCs and μEGs showed a statistically significant reduction in Z-average diameter in response to a single freeze–thaw cycle (Figure S1). Specifically, the mean Z-average of fresh RBCs was reduced from 1826 ± 211 to 648 ± 224 nm after one freeze–thaw cycle. These values underestimate the diameter of RBCs because the Z-average diameter is based on the diffusional velocity of a hypothetical hard sphere due to Brownian motion; the thin cross-section of the RBC causes its Brownian motion to be faster than that of a hard sphere with equal diameter.[52,53] For μEGs, the mean Z-average was reduced from 1454 ± 92 to 565 ± 12 nm after one freeze–thaw cycle. We attribute the reduced mean Z-average diameter values for frozen–thawed RBCs and μEGs to the respective lysates formed from these particles in response to the freeze–thaw cycle. It has been established that RBCs lyse after being frozen and thawed in isotonic saline.[54]

Lysis is often attributed to the accompanying osmotic effects during freezing and thawing.[54] When freezing slowly in an isotonic solution, the solutes (salts) are concentrated as more water is converted to ice, creating a hypertonic extracellular environment. It has been proposed that hemoglobin can be released from RBCs incubated in a hypertonic milieu through modifications made to the actin-spectrin network to cause hemoglobin leakage.[55] The hypertonic conditions experienced by the RBCs during freezing can concentrate hemoglobin within shrunken RBCs. Concentrated hemoglobin may precipitate and form a gel that creates local tensions in the membrane, leading to punctures in the membrane, causing cell lysis.[56,57]

Given that μEGs lack hemoglobin, gelation of hemoglobin would not be a basis for lysis of μEGs. During the thawing process, the intracellular expansion of ice crystals and subsequent recrystallization (where large ice crystals grow larger at the expense of smaller ones) at slow thawing rates may play a role in the freezing-induced lysis of μEGs and RBCs.[58,59] Briard et al. found that the size of the enlarged crystals that form during recrystallization can exceed 50 μm when RBCs are frozen in PBS.[58]

The diameters of ice crystals are also inversely proportional to the cooling rate in the range of about 0.06–300 °C/min (i.e., formation of larger crystals on the orders of tens of microns is associated with smaller cooling rates).[60,61] Given that our samples were cooled at a relatively slow rate (≈ -1 °C/min), we expect formation of large ice crystals that can span across multiple RBCs or μEGs, which may become even larger due to recrystallization during the thawing phase.[43,62,63] The formation of such large ice crystals may contribute to the severe disruption to the membranes of RBCs and μEGs.

The mean Z-average diameter of fresh nNETs (236.7 ± 5.7 nm) (Figure 1a) (referred to as the 0 week) was larger than that of fresh nEGs (212.4 ± 3.5 nm), and the mean diameters for these two types of particles were smaller than that of nRBCs (244.5 ± 4.4 nm). Although these differences were not statistically significant, the presence of ICG intercalated in the membrane bilayers of nNETs may give rise to a larger diameter when compared to nEGs,[2,35] and the depletion of hemoglobin from nNETs and nEGs prior to mechanical extrusion may

be the basis for their smaller diameters when compared to nRBCs.[35] In a previous study, Kuo et al. subjected "nanoerythrosomes" to five freeze–thaw cycles; each cycle consisted of freezing for 24 h at –20 °C followed by 2 h of thawing at room temperature.[39] Using DLS, they also found that the diameters of nanoerythrosomes were not affected by the cyclic freeze–thawing.

The size-stability of nanosized RBC-derived particles is likely due to their small size. It has been reported that smaller RBCs are more resistant to the osmotically driven lysis that can result from freezing.[56,64] Betticher and Geiser found that the osmotic perturbation required to release 3.5–4% of hemoglobin from RBCs was three times higher for small RBCs (31 μm^3 for sheep RBCs) when compared to larger RBCs (113 μm^3 for human newborns RBCs).[56] Similarly Peinado et al. found that the osmolality value for 50% hemolysis was about twice as high for *Capra pyrenaica* (Iberian wild goat) RBCs (4.3 μm mean cell diameter) as compared to that for *Rattus norvegicus* (Brown rat) RBCs (7.7 μm mean cell diameter).[64] Due to their smaller diameters, the nanosized RBC-derived particles have a larger surface-to-volume ratio than RBCs or μEGs, making them more resistant to changes in membrane tension (and ultimately rupture) in response to a change in volume.

The ζ values of fresh nEGs, nRBCs, and nNETs (Figure 1b) were not statistically different from that of fresh bovine RBCs (–12.1 ± 1.0 mV, data not shown). Sialoglycoproteins are associated with much of the negative charge of RBCs.[65,66] In particular, the negative surface charge can be attributed to the carboxyl groups of sialic acid (SA). Presence of SA on the membrane surface is relevant to the survival of RBCs in circulation. It has been reported that a 20–30% reduction in SA is sufficient for recognition and subsequent clearance by the reticuloendothelial system.[67,68] Storage at –20 °C for up to 8 weeks did not result in any statistically significant differences in ζ values for nEGs, nRBCs, and nNETs, when compared to their ζ values when fresh ($p > 0.05$). Therefore, our measured ζ values suggest that the negatively charged SA residues remained on the surface of RBC-derived nanoparticles even after hypotonic treatment, mechanical extrusion, and subsequent freezing/thawing.

Optical Density and Fluorescence Characteristics of Fresh and Frozen–Thawed Particles.

Spectra of frozen–thawed RBCs showed reductions in OD values as compared to those for fresh RBCs (Figure 2a). We attribute this reduction to the presence of RBC lysate after freeze–thawing, which scatters the incident light less than fresh RBCs. These results are consistent with our previous results where higher values of scattering coefficient in the spectral range of 400–1000 nm were associated with microsized NETs as compared to nanosized NETs.[69] The spectra of frozen–thawed RBCs indicated that the light-absorbing components of the RBC remained in the lysates.

The OD spectra of both fresh (0 weeks) and frozen–thawed RBCs indicated the presence of oxygenated hemoglobin as evidenced by the characteristic Q-band peaks for oxyhemoglobin at 542 and 575 nm (Figure 2a), which are respectively attributed to the fundamental absorption band (Q_0) and its vibronic tone (Q_v) for a single porphyrin $\pi \rightarrow \pi^*$ transition.[70,71] The strong Soret peak centered at 412 nm is also associated with porphyrin $\pi \rightarrow \pi^*$ transition.[70] The value of OD at this peak reached a saturating level during our

spectral recording for fresh RBCs and was >4 for the frozen–thawed RBCs. Other spectral features between 230 and 380 nm are also related to electronic transitions associated with hemoglobin absorption.[72,73]

Fresh and frozen–thawed nRBCs (positive control samples) formed by extrusion, exhibited nearly identical spectra (Figure 2b). These samples did not show or had minimal spectral peaks at the Q-band, and had a greatly reduced OD at the Soret peak, indicating that most of the hemoglobin was removed during mechanical extrusion. Centrifugal pelleting of the freshly extruded nRBCs yielded a red-colored supernatant, which indicated expulsion of hemoglobin from the nRBCs after passage through the extruder.

Fresh and frozen–thawed nEGs (negative control samples) (Figure 2c) had similar OD spectra compared to nRBCs, but lacked both the Q-band and Soret peak features associated with oxyhemoglobin that were present in RBCs and nRBCs. Therefore, the resulting spectra represent the OD due to scattering by these particles.

Similar to nEGs' spectra, the OD spectra of nNETs also lacked the absorption peaks associated with oxyhemoglobin (Figure 2d). However, nNETs spectra showed a prominent NIR peak at 807 nm due to absorption by the monomeric form of ICG and a secondary peak centered at 740 nm attributed to absorption by aggregated ICG.[35] Upon freezing-thawing, nNETs retained these NIR spectral characteristics.

In response to 720 nm photoexcitation, NIR fluorescence emitted from RBCs and nRBCs were in the noise floor (Figure 3a,b). For nNETs (Figure 3c), there was a prominent NIR fluorescence peak centered at 808 nm, associated with the monomer form of ICG. nNETs retained their NIR fluorescence for the duration of storage at −20 °C (up to 8 weeks) and upon thawing. Retention of OD and fluorescence emission over the NIR spectrum upon the freeze–thaw cycle of nNETs provide further evidence that ICG did not degrade or leak from the particles and that the particles did not lyse upon thawing. We also provide results that demonstrate that the fluorescence characteristics of nNETs remain stable in the presence of serum proteins (Figure S2).

In Vitro NIR Fluorescence Imaging and Uptake by SKOV3 Ovarian Cancer Cells.

There was minimal NIR emission from cells incubated with PBS (negative control) (Figure 4a). Fresh and frozen–thawed nNETs offered similar capability in NIR fluorescence imaging of SKOV3 ovarian cancer cells (Figure 4b,c). Both sets of particles showed similar spatial uptake by the cancer cells where they were localized at the peripheries of the cells' nuclei (stained in blue by DAPI). There were not any statistically significant differences in average NIR fluorescence emission between SKOV3 ovarian cancer cells incubated with fresh or frozen–thawed nNETs for 2 h (Figure 4d).

Biodistribution of nNETs and Frozen–Thawed nNETs in Healthy SW Mice.

In a previous study, we evaluated the biodistribution of fresh nNETs in healthy SW mice at 6, 24, and 48 h postadministration of the particles.[2] We found that accumulation of fresh nNETs in liver, spleen, lungs, and kidney continued to increase between 6 and 48 h. Therefore, in this study, we chose 18 h as a time point that would for nNETs accumulation

in these organs; hence, allowing us to determine if the biodistribution of the frozen–thawed nNETs would be significantly different from that of freshly prepared nNETs.

For both groups, there was statistically significantly higher I^* values from the spleen, which is the primary organ responsible for removing senescent RBCs from the vasculature (Figure 5).[74] The flipping of phosphatidylserine (PS) from the inner to the outer membrane leaflet of nNETs can serve as a biomarker for recognition and subsequent removal of nNETs by the macrophages spleen.[74] Using PS fluorescence immunostaining and flow cytometry, we have found that PS can become localized to the outer leaflet of nNETs, likely due to the hypotonic treatment of RBCs.[34] While nNETs with surface-exposed PS can also be recognized by the liver macrophages (Kupffer cells), they may also escape via the fenestrated endothelial lining of the liver sinusoids, then extravasate into the space of Disse, where they are eliminated from the body via the hepatobiliary system. This route of elimination may result in a lower level of nNETs (as quantified by the metric I^*) in the liver when compared to that in spleen. The alveolar and interstitial macrophages in the lungs may also uptake nNETs with surface-exposed PS, but these macrophages primarily serve to defend against pathogens, which may explain the reduced I^* in lungs, compared to spleen.[75,76] The relatively lower amount of nNETs in blood at 18 h postadministration when compared to the values for the RES organs suggests that most of the nNETs had been cleared from the vasculature by this time and had accumulated in these organs.

Using a two-way analysis of variants (ANOVA), we found no statistically significant differences between the values of I^* for fresh or frozen–thawed nNETs in blood or in the RES organs ($p < 0.05$) (see Figure 5). On the basis of their similar biodistribution profiles, as well as similar size and surface characteristics, frozen–thawed nNETs likely involve the same mechanisms for interaction with the RES as fresh nNETs.

Our results indicate that a single cycle of freezing at −20 °C followed by thawing at room temperature provides an effective method to retain the physical and optical characteristics of RBC-derived nanoparticles and their interactions with biological systems without the need for use of cryoprotectants. This freeze–thaw method may eliminate the need for just-in-time manufacturing of RBC-derived nanosized carriers and enable rapid deployment of the particles for intended clinical applications.

CONCLUSIONS

We have demonstrated that freezing of RBC-derived NIR nanoparticles, without the use of cryoprotectants, and subsequent thawing at room temperature does not alter their physical and optical properties consisting of diameter, zeta potential, optical density, and fluorescence emission. The ability of nNETs for fluorescence imaging of SKOV3 cancer cells is preserved with this storage method. We have also shown that a single cycle of freezing the nNETs to −20 °C followed by thawing at room temperature does not affect their biodistribution profile in the reticuloendothelial organs of healthy Swiss Webster mice. This widely available freeze–thaw method may provide a means for preservation and rapid deployment of RBC-derived nanoparticles for intended clinical applications.

Supplementary Material

Refer to Web version on PubMed Central for supplementary material.

ACKNOWLEDGMENTS

Funding

ABBREVIATIONS

ICG	indocyanine green
DAPI	4′,6-diamidino-2-phenylindole
nEGs	nanosized erythrocyte ghosts
NIR	near-infrared
nNETs	nanosized NIR erythrocyte-mimicking transducers
OD	optical density
RBCs	red blood cells

REFERENCES

(1). Sun L; Li Q; Hou M; Gao Y; Yang R; Zhang L; Xu Z; Kang Y; Xue P Light-Activatable Chlorin e6 (Ce6)-Imbedded Erythrocyte Membrane Vesicles Camouflaged Prussian Blue Nanoparticles for Synergistic Photothermal and Photodynamic Therapies of Cancer. Biomater. Sci 2018, 6 (11), 2881–2895. [PubMed: 30192355]

(2). Vankayala R; Mac JT; Burns JM; Dunn E; Carroll S; Bahena EM; Patel DK; Griffey S; Anvari B Biodistribution and Toxicological Evaluation of Micron- and Nano-Sized Erythrocyte-Derived Optical Particles in Healthy Swiss Webster Mice. Biomater. Sci 2019, 7 (5), 2123–2133. [PubMed: 30869663]

(3). Oldenborg PA; Zheleznyak A; Fang YF; Lagenaur CF; Gresham HD; Lindberg FP Role of CD47 as a Marker of Self on Red Blood Cells. Science 2000, 288 (5473), 2051–2054. [PubMed: 10856220]

(4). Buttari B; Profumo E; Rigano R Crosstalk Between Red Blood Cells and the Immune System and Its Impact on Atherosclerosis. BioMed Res. Int 2015, No. 616834. [PubMed: 25722984]

(5). Dalmasso AP Posttransfusion Survival of Stored Red-Cells and Membrane-Associated Complement Inhibitors. Transfusion 1993, 33 (4), 281–283. [PubMed: 8480347]

(6). Long KE; Yomtovian R; Kida M; Knez JJ; Medof ME Time-Dependent Loss of Surface Complement Regulatory Activity during Storage of Donor Blood. Transfusion 1993, 33 (4), 294–300. [PubMed: 7683151]

(7). Lichtman MA; Beutler E; Kipps TJ; Seligsohn U; Kaushansky K; Prchal J Williams Hematology, 7th ed.; McGraw-Hill Professional: New York, 2005; Vol. 487, pp 405–410.

(8). Leuzzi V; Micheli R; D'Agnano D; Molinaro A; Venturi T; Plebani A; Soresina A; Marini M; Ferremi Leali P; Quinti I; Pietrogrande MC; Finocchi A; Fazzi E; Chessa L; Magnani M Positive Effect of Erythrocyte-Delivered Dexamethasone in Ataxia-Telangiectasia. Neurol. Neuroimmunol. Neuroinflammation 2015, 2 (3), No. e98.

(9). Han X; Shen S; Fan Q; Chen G; Archibong E; Dotti G; Liu Z; Gu Z; Wang C Red Blood Cell-Derived Nanoerythrosome for Antigen Delivery with Enhanced Cancer Immunotherapy. Sci. Adv 2019, 5 (10), No. eaaw6870. [PubMed: 31681841]

(10). Magnani M; Rossi L; Fraternale A; Bianchi M; Antonelli A; Crinelli R; Chiarantini L Erythrocyte-Mediated Delivery of Drugs, Peptides and Modified Oligonucleotides. Gene Ther. 2002, 9 (11), 749–751. [PubMed: 12032702]

(11). Muzykantov VR Drug Delivery by Red Blood Cells: Vascular Carriers Designed by Mother Nature. Expert Opin. Drug Delivery 2010, 7 (4), 403–427.

(12). Markov DE; Boeve H; Gleich B; Borgert J; Antonelli A; Sfara C; Magnani M Human Erythrocytes as Nanoparticle Carriers for Magnetic Particle Imaging. Phys. Med. Biol 2010, 55 (21), 6461–6473. [PubMed: 20959685]

(13). Johnson KM; Tao JZ; Kennan RP; Gore JC Gadolinium-Bearing Red Cells as Blood Pool MRI Contrast Agents. Magn. Reson. Med 1998, 40 (1), 133–142. [PubMed: 9660563]

(14). Burns JM; Vankayala R; Mac JT; Anvari B Erythrocyte-Derived Theranostic Nanoplatforms for Near Infrared Fluorescence Imaging and Photodestruction of Tumors. ACS Appl. Mater. Interfaces 2018, 10 (33), 27621–27630. [PubMed: 30036031]

(15). Rossi L; Pierige F; Antonelli A; Bigini N; Gabucci C; Peiretti E; Magnani M Engineering Erythrocytes for the Modulation of Drugs' and Contrasting Agents' Pharmacokinetics and Biodistribution. Adv. Drug Delivery Rev 2016, 106, 73–87.

(16). Maarek JM; Holschneider DP; Harimoto J; Yang J; Scremin OU; Rubinstein EH Measurement of Cardiac Output with Indocyanine Green Transcutaneous Fluorescence Dilution Technique. Anesthesiology 2004, 100 (6), 1476–1483. [PubMed: 15166567]

(17). Lund-Johansen P The Dye Dilution Method for Measurement of Cardiac Output. Eur. Heart J 1990, 11, 6–12. [PubMed: 2092991]

(18). Hoekstra LT; de Graaf W; Nibourg GA; Heger M; Bennink RJ; Stieger B; van Gulik TM Physiological and Biochemical Basis of Clinical Liver Function Tests: A Review. Ann. Surg 2013, 257 (1), 27–36. [PubMed: 22836216]

(19). Shinohara H; Tanaka A; Kitai T; Yanabu N; Inomoto T; Satoh S; Hatano E; Yamaoka Y; Hirao K Direct Measurement of Hepatic Indocyanine Green Clearance with Near-Infrared Spectroscopy: Separate Evaluation of Uptake and Removal. Hepatology 1996, 23 (1), 137–144. [PubMed: 8550033]

(20). Keiding S Hepatic Clearance and Liver Blood Flow. J. Hepatol 1987, 4 (3), 393–398. [PubMed: 3298417]

(21). Baillif S; Wolff B; Paoli V; Gastaud P; Mauget-Faysse M Retinal Fluorescein and Indocyanine Green Angiography and Spectral-Domain Optical Coherence Tomography Findings in Acute Retinal Pigment Epitheliitis. Retina 2011, 31 (6), 1156–1163. [PubMed: 21293312]

(22). Bearelly S; Espinosa-Heidmann DG; Cousins SW The Role of Dynamic Indocyanine Green Angiography in the Diagnosis and Treatment of Retinal Angiomatous Proliferation. Br. J. Ophthalmol 2008, 92 (2), 191–196. [PubMed: 17962393]

(23). Cohen SM Indocyanine Green Angiography of a Laser-Induced Retinal-Choroidal Venous Anastomosis. Ophthalmic Surg. Lasers 1997, 28 (1), 65–66. [PubMed: 9031308]

(24). Wolf S; Remky A; Elsner AE; Arend O; Reim M Indocyanine Green Video Angiography in Patients with Age-Related Maculopathy-Related Retinal Pigment Epithelial Detachments. Ger. J. Ophthalmol 1994, 3 (4–5), 224–227. [PubMed: 7528587]

(25). Zhang X; Li Y; Zhou Y; Mao F; Lin Y; Guan J; Sun Q Diagnostic Performance of Indocyanine Green-Guided Sentinel Lymph Node Biopsy in Breast Cancer: A Meta-Analysis. PLoS One 2016, 11 (6), No. e0155597. [PubMed: 27280407]

(26). Pitsinis V; Provenzano E; Kaklamanis L; Wishart GC; Benson JR Indocyanine Green Fluorescence Mapping for Sentinel Lymph Node Biopsy in Early Breast Cancer. Surg. Oncol 2015, 24 (4), 375–379. [PubMed: 26555151]

(27). Namikawa K; Yamazaki N Sentinel Lymph Node Biopsy Guided by Indocyanine Green Fluorescence for Cutaneous Melanoma. Eur.J. Dermatol 2011, 21 (2), 184–190. [PubMed: 21498148]

(28). Hayashi T; Furukawa H; Oyama A; Funayama E; Saito A; Yamao T; Yamamoto Y Sentinel Lymph Node Biopsy using Real-Time Fluorescence Navigation with Indocyanine Green in Cutaneous Head and Neck/Lip Mucosa Melanomas. Head Neck 2012, 34 (5), 758–761. [PubMed: 21246639]

(29). Cacciamani GE; Shakir A; Tafuri A; Gill K; Han J; Ahmadi N; Hueber PA; Gallucci M; Simone G; Campi R; Vignolini G; Huang WC; Taylor J; Becher E; Van Leeuwen FWB; Van Der Poel HG; Velet LP; Hemal AK; Breda A; Autorino R; Sotelo R; Aron M; Desai MM; De Castro Abreu AL Best Practices in Near-Infrared Fluorescence Imaging with Indocyanine Green (NIRF/ICG)-Guided Robotic Urologic Surgery: A Systematic Review-Based Expert Consensus. World J. Urol 2020, 38, 883–896. [PubMed: 31286194]

(30). Namikawa T; Sato T; Hanazaki K Recent Advances in Near-Infrared Fluorescence-Guided Imaging Surgery using Indocyanine Green. Surg. Today 2015, 45 (12), 1467–1474. [PubMed: 25820596]

(31). DSouza AV; Lin H; Henderson ER; Samkoe KS; Pogue BW Review of Fluorescence Guided Surgery Systems: Identification of Key Performance Capabilities Beyond Indocyanine Green Imaging. J. Biomed. Opt 2016, 21 (8), No. 080901. [PubMed: 27533438]

(32). Bahmani B; Bacon D; Anvari B Erythrocyte-Derived Photo-Theranostic Agents: Hybrid Nano-Vesicles Containing Indocyanine Green for Near Infrared Imaging and Therapeutic Applications. Sci. Rep 2013, 3, No. 2180. [PubMed: 23846447]

(33). Burns JM; Jia WC; Nelson JS; Majaron B; Anvari B Photothermal Treatment of Port-Wine Stains using Erythrocyte-Derived Particles Doped with Indocyanine Green: A Theoretical Study. J. Biomed. Opt 2018, 23 (12), No. 121616. [PubMed: 30499264]

(34). Jia W; Burns JM; Villantay B; Tang JC; Vankayala R; Lertsakdadet B; Choi B; Nelson JS; Anvari B Intravital Vascular Phototheranostics and Real-Time Circulation Dynamics of Micro- and Nanosized Erythrocyte-Derived Carriers. ACS Appl Mater. Interfaces 2020, 12 (1), 275–287. [PubMed: 31820920]

(35). Tang JC; Partono A; Anvari B Near-Infrared-Fluorescent Erythrocyte-Mimicking Particles: Physical and Optical Characteristics. IEEE Trans. Biomed. Eng 2019, 66 (4), 1034–1044. [PubMed: 30130175]

(36). Sparrow RL Red Blood Cell Storage and Transfusion-Related Immunomodulation. Blood Transfus. 2010, 8, No. s26–30. [PubMed: 20606746]

(37). Chaudhari CN Frozen Red Blood Cells in Transfusion. Med. J. Armed Forces India 2009, 65 (1), 55–58. [PubMed: 27408192]

(38). Chaplin H Jr. The Proper Use of Previously Frozen Red-Blood-Cells for Transfusion. Blood 1982, 59 (6), 1118–1120. [PubMed: 7082817]

(39). Kuo YC; Wu HC; Hoang D; Bentley WE; D'Souza WD; Raghavan SR Colloidal Properties of Nanoerythrosomes Derived from Bovine Red Blood Cells. Langmuir 2016, 32 (1), 171–179. [PubMed: 26684218]

(40). Nalbant D; Cancelas JA; Mock DM; Kyosseva SV; Schmidt RL; Cress GA; Zimmerman MB; Strauss RG; Widness JA In Premature Infants there is No Decrease in 24-h Posttransfusion Allogeneic Red Blood Cell Recovery after 42 Days of Storage. Transfusion 2018, 58 (2), 352–358. [PubMed: 29193118]

(41). Mac JT; Nunez V; Burns JM; Guerrero YA; Vullev VI; Anvari B Erythrocyte-Derived Nano-Probes Functionalized with Antibodies for Targeted Near Infrared Fluorescence Imaging of Cancer Cells. Biomed. Opt. Express 2016, 7 (4), 1311–1322. [PubMed: 27446657]

(42). Mac JT; Vankayala R; Patel DK; Wueste S; Anvari B Erythrocyte-Derived Optical Nanoprobes Doped with Indocyanine Green-Bound Albumin: Material Characteristics and Evaluation for Cancer Cell Imaging. ACS Biomater. Sci. Eng 2018, 4 (8), 3055–3062. [PubMed: 33435025]

(43). Baboo J; Kilbride P; Delahaye M; Milne S; Fonseca F; Blanco M; Meneghel J; Nancekievill A; Gaddum N; Morris GJ The Impact of Varying Cooling and Thawing Rates on the Quality of Cryopreserved Human Peripheral Blood T Cells. Sci. Rep 2019, 9, No. 3417. [PubMed: 30833714]

(44). Tang JB; Erdener SE; Li BQ; Fu BY; Sakadzic S; Carp SA; Lee JW; Boas DA Shear-Induced Diffusion of Red Blood Cells Measured with Dynamic Light Scattering-Optical Coherence Tomography. J. Biophotonics 2018, 11 (2), No. e201700070.

(45). Mauer J; Peltomaki M; Poblete S; Gompper G; Fedosov DA Static and Dynamic Light Scattering by Red Blood Cells: A Numerical Study. PLoS One 2017, 12 (5), No. e0176799. [PubMed: 28472125]

(46). Hohl A; Ramms AS; Dohmen C; Mantwill K; Bielmeier A; Kolk A; Ruppert A; Nawroth R; Holm PS Adenovirus Particle Quantification in Cell Lysates Using Light Scattering. Hum. Gene Ther: Methods 2017, 28 (5), 268–276. [PubMed: 28806885]

(47). Zhang Q; Honko A; Zhou J; Gong H; Downs SN; Vasquez JH; Fang RH; Gao W; Griffiths A; Zhang L Cellular Nanosponges Inhibit SARS-CoV-2 Infectivity. Nano Lett. 2020, 20 (7), 5570–5574. [PubMed: 32551679]

(48). Carvalho PM; Felicio MR; Santos NC; Goncalves S; Domingues MM Application of Light Scattering Techniques to Nanoparticle Characterization and Development. Front. Chem 2018, 6, No. 237. [PubMed: 29988578]

(49). Koppel DE Analysis of Macromolecular Polydispersity in Intensity Correlation Spectroscopy - Method of Cumulants. J. Chem. Phys 1972, 57 (11), 4814–4820.

(50). Thomas JC The Determination of Log Normal Particle-Size Distributions by Dynamic Light-Scattering. J. Colloid Interface Sci 1987, 117 (1), 187–192.

(51). Schnitzer O; Zeyde R; Yavneh I; Yariv E Weakly Nonlinear Electrophoresis of a Highly Charged Colloidal Particle. Phys. Fluids 2013, 25 (5), No. 052004.

(52). Hassan PA; Rana S; Verma G Making Sense of Brownian Motion: Colloid Characterization by Dynamic Light Scattering. Langmuir 2015, 31 (1), 3–12. [PubMed: 25050712]

(53). Pecora R Dynamic Light Scattering Measurement of Nanometer Particles in Liquids. J. Nanopart. Res 2000, 2 (2), 123–131.

(54). Lovelock JE The Haemolysis of Human Red Blood-Cells by Freezing and Thawing. Biochim. Biophys. Acta 1953, 10 (3), 414–426. [PubMed: 13058999]

(55). Heubusch P; Jung CY; Green FA The Osmotic Response of Human-Erythrocytes and the Membrane Cytoskeleton. J. Cell. Physiol 1985, 122 (2), 266–272. [PubMed: 3918046]

(56). Betticher DC; Geiser J Resistance of Mammalian Red Blood Cells of Different Size to Hypertonic Milieu. Comp. Biochem. Physiol. Part A: Physiol 1989, 93 (2), 429–432.

(57). Ponder E Hemolysis and Related Phenomena. Grune & Stratton: New York, 1971.

(58). Briard JG; Poisson JS; Turner TR; Capicciotti CJ; Acker JP; Ben RN Small Molecule Ice Recrystallization Inhibitors Mitigate Red Blood Cell Lysis during Freezing, Transient Warming and Thawing. Sci. Rep 2016, 6, No. 23619. [PubMed: 27021850]

(59). Baust JM Molecular Mechanisms of Cellular Demise Associated with Cryopreservation Failure. Cell Preserv. Technol 2002, 1 (1), 17–31.

(60). Asghar W; El Assal R; Shafiee H; Anchan RM; Demirci U Preserving Human Cells for Regenerative, Reproductive, and Transfusion Medicine. Biotechnol. J 2014, 9 (7), 895–903. [PubMed: 24995723]

(61). van der Sman RGM; Voda A; van Dalen G; Duijster A Ice Crystal Interspacing in Frozen Foods. J. Food Eng 2013, 116 (2), 622–626.

(62). Fowler A; Toner M Cryo-Injury and Biopreservation. Ann. N. Y. Acad. Sci 2005, 1066, 119–135. [PubMed: 16533923]

(63). Chaytor JL; Tokarew JM; Wu LK; Leclere M; Tam RY; Capicciotti CJ; Guolla L; von Moos E; Findlay CS; Allan DS; Ben RN Inhibiting Ice Recrystallization and Optimization of Cell Viability after Cryopreservation. Glycobiology 2012, 22 (1), 123–133. [PubMed: 21852258]

(64). Peinado VI; Viscor G; Palomeque J Erythrocyte Osmotic Fragility in Some Artiodactylid Mammals - Relationships with Plasma Osmolality and Red-Cell Dimensions. Comp. Haematol. Int 1992, 2 (1), 44–50.

(65). Rogers ME; Williams DT; Niththyananthan R; Rampling MW; Heslop KE; Johnston DG Decrease in Erythrocyte Glycophorin Sialic-Acid Content Is Associated with Increased Erythrocyte Aggregation in Human Diabetes. Clin. Sci 1992, 82 (3), 309–313.

(66). Huang YX; Wu ZJ; Mehrishi J; Huang BT; Chen XY; Zheng XJ; Liu WJ; Luo M Human Red Blood Cell Aging: Correlative Changes in Surface Charge and Cell Properties. J. Cell. Mol. Med 2011, 15 (12), 2634–2642. [PubMed: 21435169]

(67). Kahane I; Polliack A; Rachmilewitz EA; Bayer EA; Skutelsky E Distribution of Sialic Acids on the Red Blood Cell Membrane in Beta Thalassaemia. Nature 1978, 271 (5646), 674–675. [PubMed: 625337]

(68). Durocher JR; Payne RC; Conrad ME Role of Sialic Acid in Erythrocyte Survival. Blood 1975, 45 (1), 11–20. [PubMed: 803103]

(69). Burns JM; Saager R; Majaron B; Jia WC; Anvari B Optical Properties of Biomimetic Probes Engineered from Erythrocytes. Nanotechnology 2017, 28 (3), No. 035101. [PubMed: 27966473]

(70). Cordone L; Cupane A; Leone M; Vitrano E Optical Absorption Spectra of Deoxy- and Oxyhemoglobin in the Temperature Range 300–20 K. Relation with Protein Dynamics. Biophys. Chem 1986, 24 (3), 259–275. [PubMed: 3768470]

(71). Eaton WA; Hanson LK; Stephens PJ; Sutherland JC; Dunn JBR Optical-Spectra of Oxy-Hemoglobin and Deoxyhemoglobin. J. Am. Chem. Soc 1978, 100 (16), 4991–5003.

(72). Jacques SL Optical Properties of Biological Tissues: A Review. Phys. Med. Biol 2013, 58 (11), R37–R61. [PubMed: 23666068]

(73). Nonoyama A; Garcia-Lopez A; Garcia-Rubio LH; Leparc GF; Potter RL Hypochromicity in Red Blood Cells: An Experimental and Theoretical Investigation. Biomed. Opt. Express 2011, 2 (8), 2126–2143. [PubMed: 21833353]

(74). Mebius RE; Kraal G Structure and Function of the Spleen. Nat. Rev. Immunol 2005, 5 (8), 606–616. [PubMed: 16056254]

(75). Byrne AJ; Mathie SA; Gregory LG; Lloyd CM Pulmonary Macrophages: Key Players in the Innate Defence of the Airways. Thorax 2015, 70 (12), 1189–1196. [PubMed: 26286722]

(76). Koch CM; Chiu SF; Misharin AV; Ridge KM Lung Interstitial Macrophages: Establishing Identity and Uncovering Heterogeneity. Am. J. Respir. Cell Mol. Biol 2017, 57 (1), 7–9. [PubMed: 28665216]
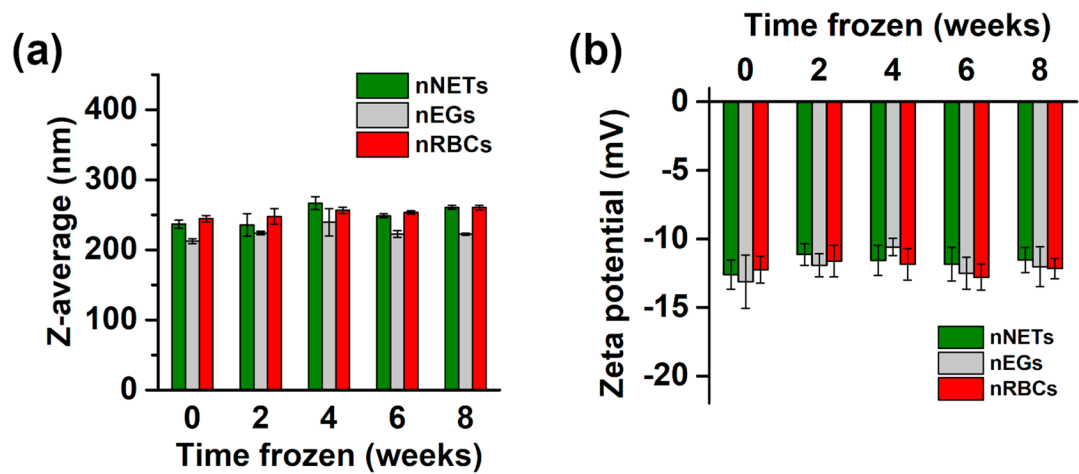
Figure 1.
Mean values of the (a) Z-average diameters, and (b) the zeta potentials (ζ) for fresh (frozen for 0 weeks) and frozen–thawed nNETs, nEGs, and nRBCs for various durations of frozen storage at −20 °C. In all panels, error bars are the standard deviations associated with eight independent measurements of the same sample. All measurements were made in 1× PBS.
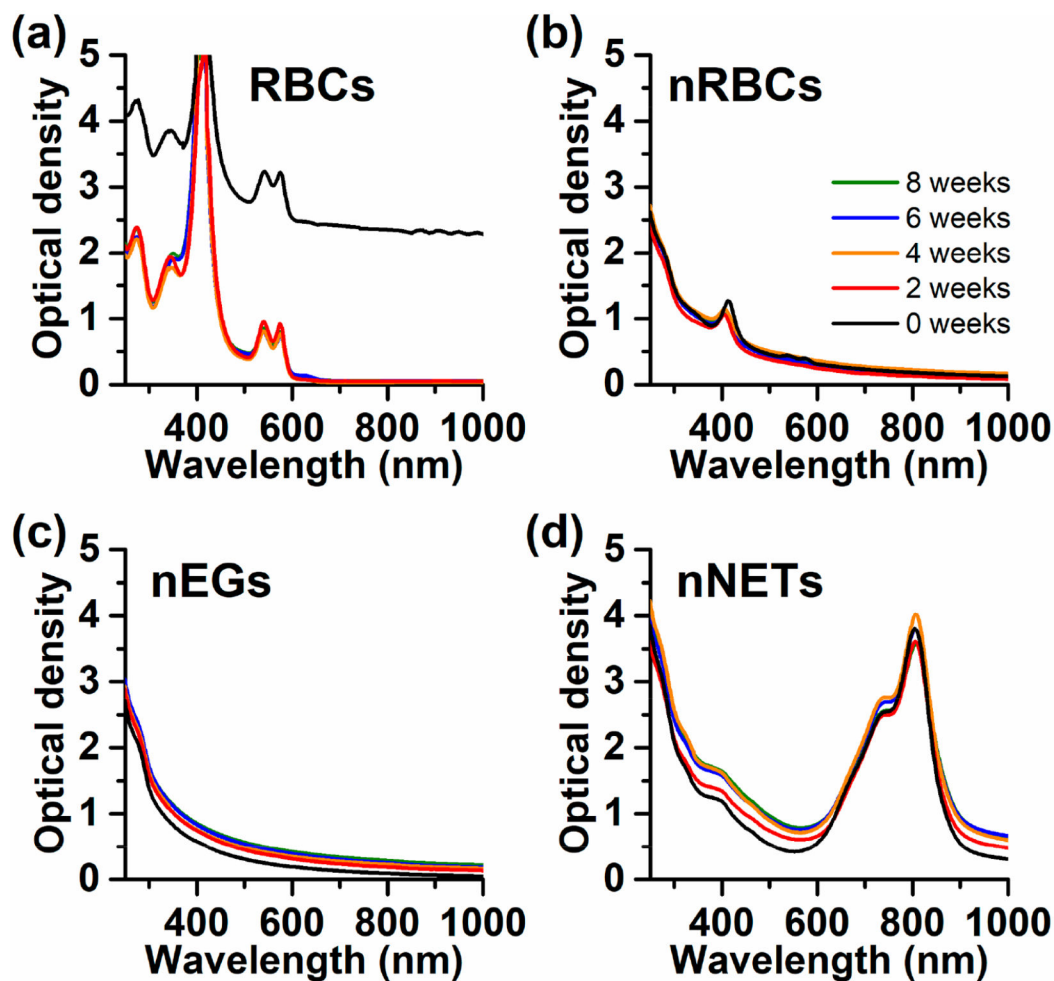
Figure 2.
Optical density spectra for fresh and frozen–thawed samples of (a) RBCs, (b) nRBCs, (c) nEGs, and (d) nNETs after −20 °C storage for up to 8 weeks. All spectra were obtained with samples suspended in 1× PBS. Legends shown on panel (b) apply to all panels.
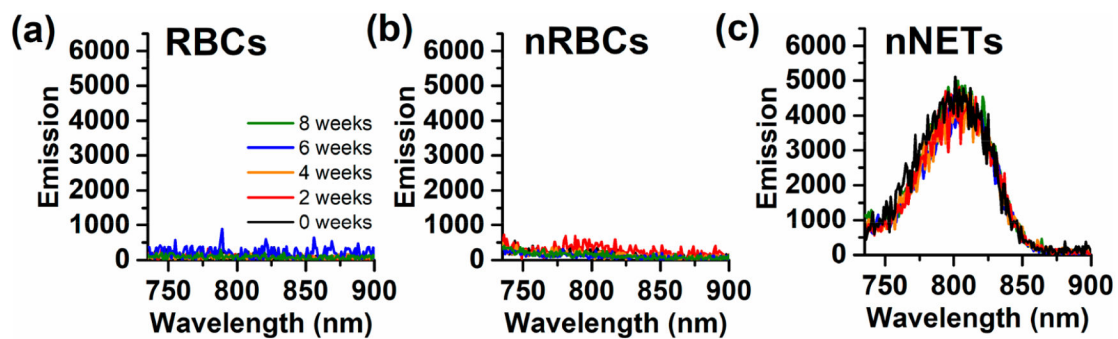
Figure 3.
Fluorescence emission of (a) RBCs, (b) nRBCs, and (c) nNETs after storage for up to 8 weeks at −20 °C. The legend in panel (a) applies to all panels. Excitation wavelength was 720 nm and spectral recordings were made with samples suspended in 1× PBS.
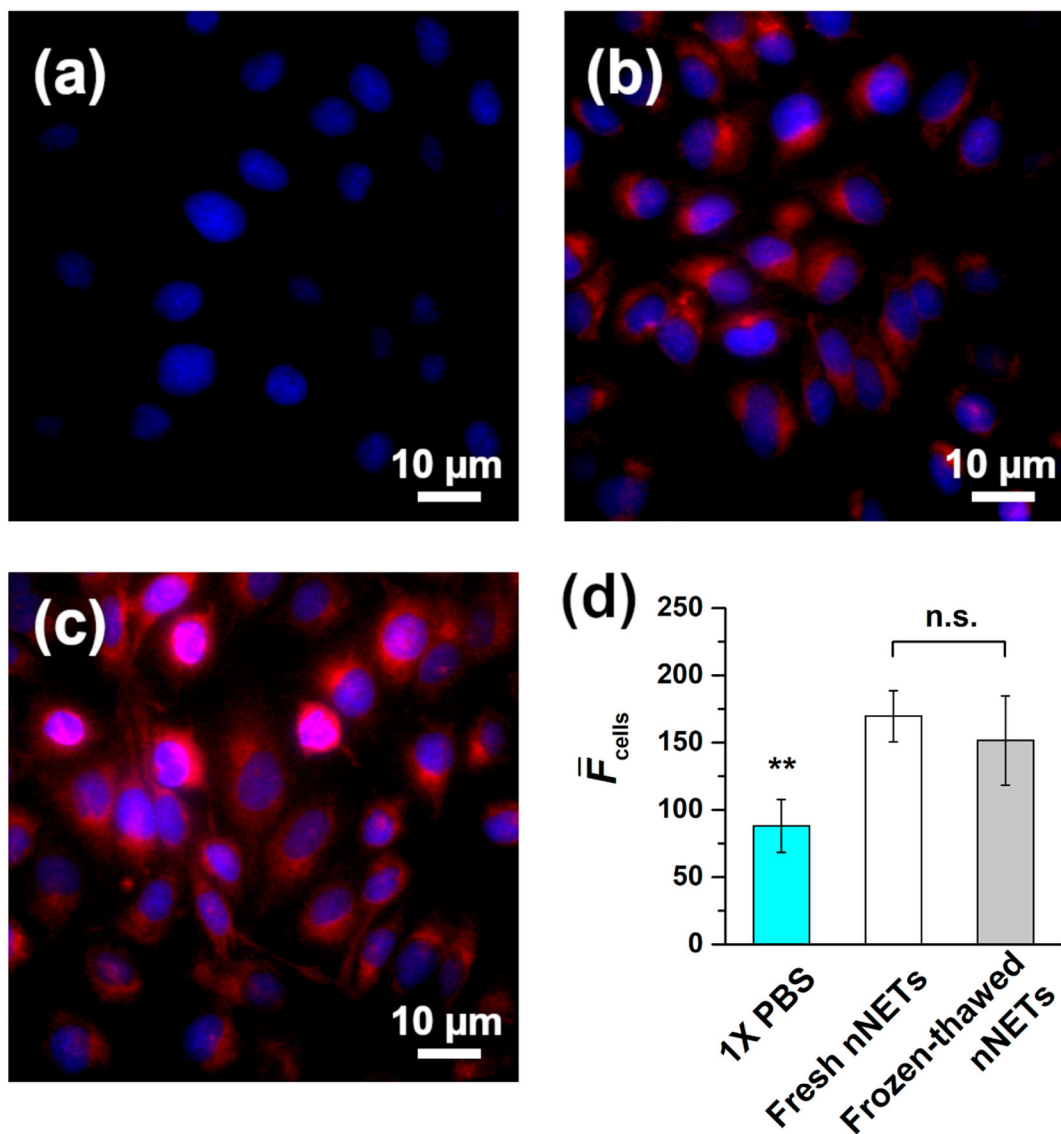
Figure 4.
Fluorescence images of SKOV3 ovarian cancer cells after 2 h of incubation at 37 °C with (a) 1× PBS, (b) fresh nNETs, and (c) frozen–thawed nNETs. Blue and red channels represent DAPI and ICG emission, respectively. In panel (d), we show the average cell fluorescence ($\overline{F}_{cells}$, see eq 1) of SKOV3 cells incubated with 1× PBS, fresh nNETs, or frozen–thawed nNETs ($n = 4$ sets of images). n.s. indicates no statistically significant difference between fresh and frozen–thawed nNETs ($p > 0.05$). Double asterisk symbol indicates significance level of $p < 0.01$ for 1× PBS compared to either fresh or frozen–thawed nNETs.
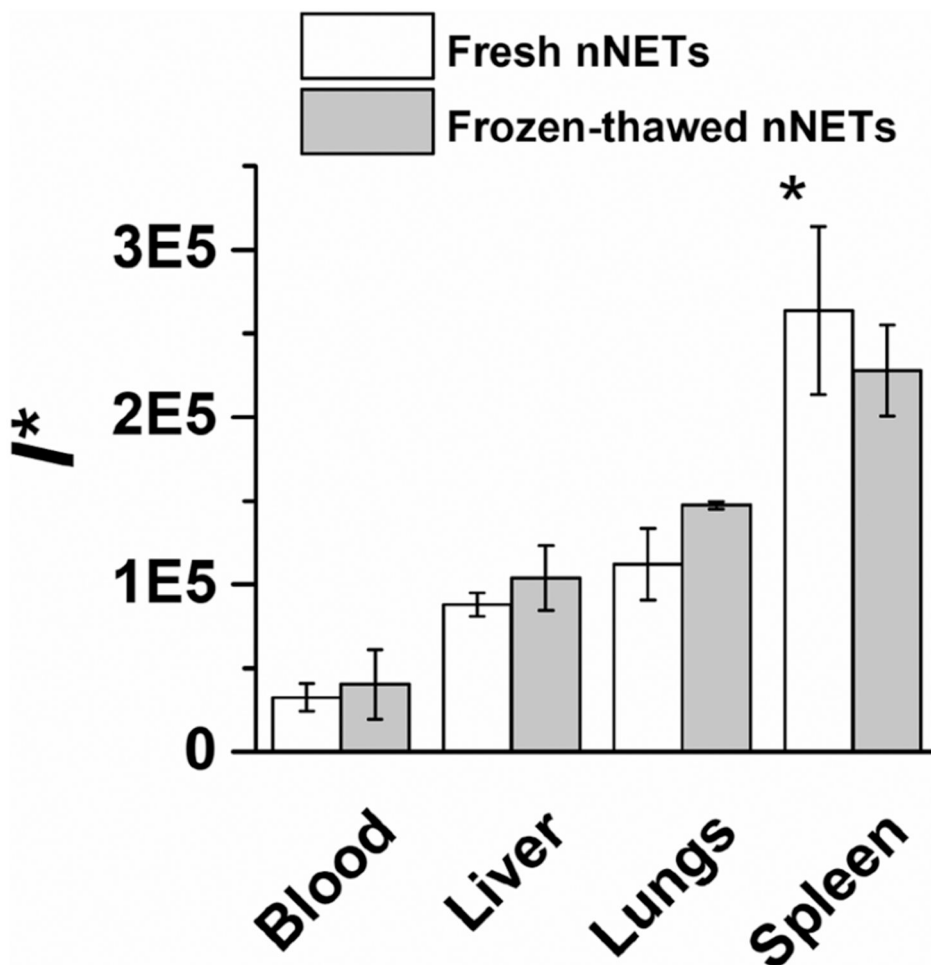
Figure 5.

Values of I^* (see eq 2) associated with blood, liver, lungs, and spleen of healthy SW mice at 18 h post tail-vein injection of fresh or frozen–thawed nNETs ($n = 3$). Error bars represent standard deviations from the mean values of I^*. Asterisk indicates that the values of I^* associated with spleen in response to injection of both fresh and frozen–thawed nNETs were significantly higher ($p > 0.05$) than the values in blood and other organs.